21st European Conference on Fracture, ECF21, 20-24 June 2016, Catania, Italy

Influence of nominal composition variation on phase evolution and creep life of Type 316H austenitic stainless steel components

Ana I. Martinez-Ubeda[a]*, Ian Griffiths[b], Mudith S. A. Karunaratne[c], Peter E. J. Flewitt[b], Charles Younes[a], Tom Scott[a]

[a]*Interface Analysis Centre, HH Wills Laboratory, University of Bristol, Bristol BS8 1TL, UK*
[b]*School of Physics, HH Wills Laboratory, University of Bristol, Bristol BS8 1FD, UK*
[c]*Department of Materials, Loughborough University, Loughborough, LE11 3TU, UK*

Abstract

The present work aims to understand the influence of variation in chemical composition in the long term evolution of secondary phases. Three samples with nominal composition of Type 316H but different specific composition have been exposed to 505ºC during 150, 145 and 300 kh. The percentage of ferrite and $M_{23}C_6$ carbide have been measured using EBSD and compared with Thermo-Calc predictions. In addition, thin foils were prepared and characterized to identify secondary phases in the samples. The discussion is focused on the influence of the secondary phases on creep deformation and failure.

Keywords: 316H austentic stainless steel; creep cavitation; creep deformation; phase transformation;

1. Introduction

In the United Kingdom to maintain the power supply a generation of Advances Cooled Gas Reactors (AGR) need to have an extended working life compared with the initial design life to build the bridges between the old and the new nuclear power plant. To achieve this, it is important to have a clear understanding of the degradation of components fabricated from AISI Type 316H austenite stainless steel, mainly within the boiler including headers, pipes and tubes. These components operate at temperatures about 550ºC where creep life is important. Creep cavitation has been seen

---

* Corresponding author. Tel.: +44 7583542093.
  E-mail address: Ana.Martinez@bristol.ac.uk

to coarse producing cracks following grain boundaries in the heat affective zone (HAZ) of boiler superheater bifurcations (Martinez-Ubeda et al, 2016). Various interactive factors contribute to creep deformation and fracture and these have to be taken into account when evaluating service life.

Different secondary phases evolve in Type 316H stainless steel during long term ageing and service (Padilha & Rios, 2002), including α-ferrite, carbides and intermetallic phases (Padilha & Rios, 2002; Lo et al, 2009; Lai, 1983; Senior,1990). Carbides $M_{23}C_6$ and M_6C, where M is Fe, Cr, Ni or Mo, have been identified in 316H austenitic stainless steel but other types like M_7C_3, or MC may also evolve depending on the specific composition (Padilha & Rios, 2002). The kinetics and type of precipitates formed depend upon several factors including the specific composition of the material, the magnitude of the service stresses and the local composition.

The number, distribution and type of precipitates control creep life, since secondary phase precipitate evolution modifies creep rate (Intrater & Machlin, 1959; Challenger & Moteff, 1973; Warren et al, 2015). Such precipitates can lead to a reduction in creep deformation by pining dislocations (Lo et al, 2009; Lai, 1983; Hsieh & Wu, 2012). Moreover, creep cavitation have been associated with inter-granular precipitation (Hsieh & Wu,2012; Dyson, 1983) such as α/δ-ferrite (Warren et al, 2015), which modify creep failure. It is also recognized that intermetallic phases such as sigma and chi degrade creep life (Intrater & Machlin, 1959; Senior, 1990). In addition, Dyson (1983) proposed a relationship relating the density of grain boundary precipitates, N_p, with creep cavity number density, N_a,

$$N_a = f \, N_p (1 - exp^{-k \, \varepsilon})$$
(1)

where f is function of interfacial energy and maximum principal stress, k is a measure of the cavity interaction and ε is the strain. The critical radius for cavity nucleation can be expressed (Dyson, 1983)

$$r = 2\gamma'/\sigma$$
(2)

where r is the cavity radius, γ' is the interfacial energy and σ is the local tensile stress normal to the grain boundary. In equation (1) the density controls the formation of cavities. However it has to be recognized that this depends upon the type of precipitate and the specific interfacial energy (Seah, 1979). While some precipitates may promote the nucleation of creep cavities, others retard creep cavity nucleation because the interfacial energy is not appropriate and their presence reduces the ability of the grain boundaries to slide (Intrater & Machlin, 1959; Seah, 1979). According to equation (2) any decrease in the interfacial energy (e.g. impurity segregation) leads to a decrease in the critical cavity radius so that nucleation process is facilitated.
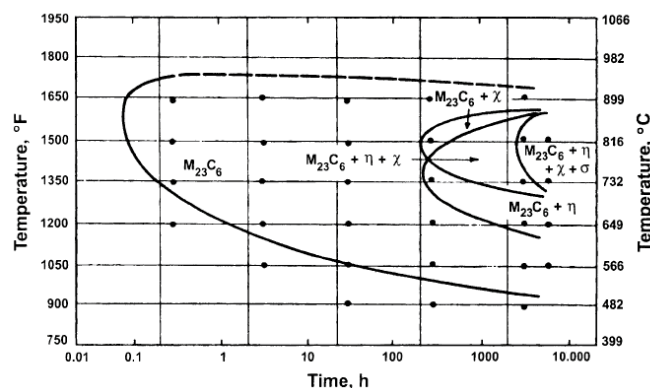

Fig. 1. TTT diagram of Type AISI 316 austenitic stainless steel, solution annealed for 1.5 h at 1260°C and water quenched prior to aging (Weiss & Strickler, 1972).

Time-temperature-transformation/precipitation diagrams (TTT/TTP) show the sequence of precipitation and the competition among different phases. Phase diagrams and the TTT curves are both function of the specific composition (nominal composition given by the AISI standards) and, as a consequence, they vary from cast to cast. Figure 1 shows the TTT diagram of Type AISI 316 austenitic stainless steel, solution annealed for 1.5 h at 1260°C and water quenched

prior to aging (Weiss & Strickler, 1972). It is not clear whether the precipitates keep transforming after times after 10,000 hours because there are little experiments data after such a longer times. Computer modeling to predict equilibrium phase diagram, precipitation processes and sequence of precipitation, are becoming increasingly important. For example, Thermo-Calc based on CALPHAD method are able to simulate equilibrium phase diagrams for multicomponent systems.

In this work we compare statistically the main chemical elements measured for three samples of Type 316H austenite stainless steel to identify significant differences in composition. Then we compare hardness, percentage of secondary phases $M_{23}C_6$ and ferrite measured experimentally with equilibrium computer simulation (Thermo-Calc). The influence of composition to the secondary phase evolution is discussed with respect to creep life.

2. Materials and experimental methods

2.1. Materials

Three ex-service tubes A, B and C were provided by EDF Energy Ltd. The three samples were in service for 150, 145 and 300 kh respectively at a temperature of approximately 505°C. A section of each tube was extracted, encapsulated in conductive resin and metallurgicaly prepared up to ¼ µm polishing paste and then vibropolished with silica suspension solution. Their specific composition was determined in parent (away from HAZ) using a JEOL 8530F field emission (FEG) electron probe microanalyses (EPMA) using 15kV, 100 nA and probe diameter of 15µm. The system was equipped with five wavelength dispersive spectrometers (WDS) and an energy dispersive spectrometer (EDS). Table 1 shows the mean of 20 to 25 point analyses and the standard deviation used here as the error. Wet analyses were provided for samples A and B, their values given in brackets in Table 1, are in good agreement with the EPMA measured compositions.

The chemical composition of the three samples were statistically compared using SPSS statistics software (Field, 2013). To compare the three samples, the whole population of EPMA data analysis have been used. First, the normality Kolmogorov-Smirnov (K-S) and Shapiro-Wilkinson (S-W) tests were carried out to stablish if the values of each chemical element were normal-distributed (Razali & Wah, 2011). Later, parametric tests were be used to compare the samples. ANOVA test compared the mean of each chemical element within the three samples to identify significant differences between them. To elucidate which ones are different from each other, LSD (least significant difference) and Bonferroni multiple comparison test were undertaken (Field, 2013).

Table 1. Mean of 20-25 EPMA analyses of chemical composition of the parent metal. Wet analysis shown in brackets.

		Wt%								
		Si	Ni	Cr	Mn	Mo	C	P	S	Fe
Sample	A	0.45±0.01 (0.41)	11.48±0.31 (11.70)	16.21±0.23 (16.6)	1.43±0.04 (1.47)	2.34±0.10 (2.43)	0.05± (0.05)	0.04±0.01 (0.02)	0.02±0.02 (0.01)	balance
	B	0.64±0.02 (0.63)	13.59±0.06 (14.12)	15.80±0.16 (16.55)	1.74±0.03 (1.78)	2.14±0.07 (2.35)	0.06± (0.06)	0.03±0.01 (0.04)	0.02±0.02 (0.01)	balance
	C	0.59±0.06	14.07±0.26	16.49±0.49	1.19±0.07	2.04±0.32	0.07±	0.03±0.01	0.04±0.01	balance

2.2. Characterisation

To quantify the amount of $M_{23}C_6$ and ferrite after long term ageing, electron backscattered diffraction (EBSD) maps covering similar 100x100 µm areas were prepared using a Zeiss Sigma HD VP field emission scanning electron microscope (SEM) operating at 30kV with 120 µm aperture and 0.3 µm step size. OIM Data Collection Software was used to analyze the maps and percentages of ferrite and carbide was acquired for the same area maps. Thermodynamic calculations were performed using Thermo-Calc (Version 2015b) with TCFE Steels/Fe-Alloys thermodynamic database (Version 7) and the results were compared with EBSD observations.

Thin foils containing a grain boundary were prepared from parent of the three samples by the focused gallium ion beam milling lift out technique (Giannuzzi & Stevie, 1999) using a FEI Helios NanoLab 600 (dual beam workstation). Composition and electron diffraction patterns of grain boundary precipitates were obtained using a JEOL ARM-200F high resolution instrument operating at 200kV and fitted with a JEOL energy dispersive X-ray spectrometer.

Finally, hardness profiles of the three samples were undertaken using a Micro-Met 6030 (Buheler) Vickers micro-hardness indenter with 0.1 kg load.

3. Results

The mean of the EPMA chemical analysis for samples A, B and C, are shown in Table 1. Only the main elements (Si, Ni, Cr, Mn, Mo and Fe) were statistically compared. The normalization, ANOVA and multiple comparison statistical tests were carried out using the whole sample population of each element analyzed, working at 0.95 confidence level (0.05 significance level). K-S and S-W normality tests confirmed the distribution of the EPMA values obtained for each element was normal for each sample except for Mn in sample A. The results of ANOVA test reveals that the content of each element is significant different between the three samples. Table 2 shows the results of fthe multiple comparison tests, LSD and Bonferroni. The samples A-C are similar in Cr content and the samples B-C are similar in Fe and Mo content. The rest of the possible pairs of samples are different for every considered element, as can be seen in Table 2. The actual difference value is included next to the corresponding element for every possible pair of samples (top sample minus left sample, the negative value indicates the top sample is of a lower concentration for this element).

The silicon content is significantly different between the three samples, with the greatest difference between samples A and B (-0.20 wt%). Cr content is significantly different between samples A–B and B-C (0.41wt% and -0.69 wt% respectively) whereas sample A-C are similar. Mn content is significantly different between the three samples with the biggest difference between samples B-C (0.55 wt%). In the case of Fe, samples A-B and A-C are significantly different (1.88 and 1.73 wt%) while B-C are similar (-0.18 wt%). Ni content is significantly different between all possible sample combination with the highest difference between sample A-C (-2.59 wt%) followed by A-B (-2.11 wt%). Mo content is significantly similar between samples B-C but different between samples A-B and A-C (0.20 and 0.30 wt%). These differences are important since these AISI Type 316H austenitic stainless steels are prepared to the same nominal composition.

Micro-hardness profiles with 100 g load were undertaken on the three samples. Their average values are 171.8 Hv for sample A, 196.6 for sample B and 202.2 for sample C. Sample A has a lower hardness value than B and C.

EBSD maps for similar size-area reveal in sample A 0.3% ferrite and 0.2% $M_{23}C_6$, in sample B ferrite and $M_{23}C_6$ 0.3% for both phases, and in sample C ferrite is 0.4% and $M_{23}C_6$ is 0.3%. Figure 2 shows an example of EBSD map for sample B.

Table 2: Multiple comparison test and mean differences between pair of samples for each element in the study. An element is highlighted only when there are not significant differences between samples. The sample difference (top sample minus left) is expressed in wt%.

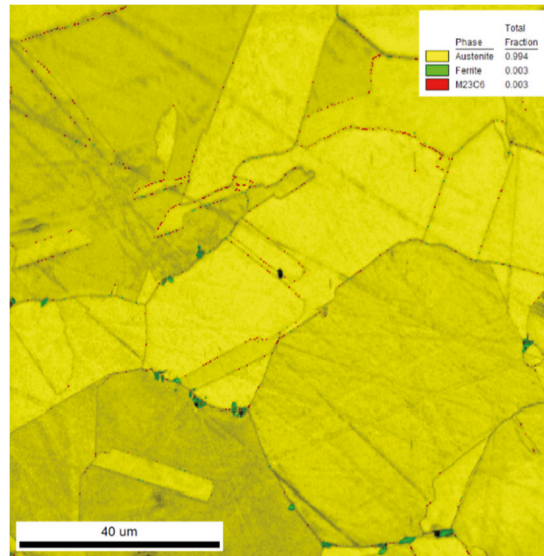|	A				B			
B	Si	-0.20	Fe	1.88				
	Cr	0.41	Ni	-2.11				
	Mn	-0.32	Mo	0.20				
C	Si	-0.14	Fe	1.73	Si	0.06	Fe	-0.14
	Cr	-0.28	Ni	-2.59	Cr	-0.69	Ni	-0.48
	Mn	0.23	Mo	0.30	Mn	0.55	Mo	0.10

Fig. 2. EBSD map of sample B showing $M_{23}C_6$ and ferrite distribution in the austenite matrix (legend based on the unit)

Inter-granular microstructure was obtained analyzing the TEM specimens extracted from the parent of each sample. Three different secondary phases were identified α/δ-ferrite, $M_{23}C_6$ and a high silicon phase (potentially G or R phase). Figure 3 a) shows a dark field TEM image with a cavity inside (dark contrast) with selected diffraction pattern (Figure 3b), position 1 shows $M_{23}C_6$ with a face centered cubic (fcc) structure and lattice parameter 10.73Å (zone axis [0 1 1]), position 2 shows α/δ-ferrite with a body center cubic (bcc) structure and lattice parameter 2.78 Å (zone axis [0 0 1]). EDS map provided the composition of both types of precipitates. The distribution of main alloying elements were consistent with literature data (Padilha & Rios, 2002), $M_{23}C_6$ was rich in chromium but depleted in nickel and the α/δ ferrite was depleted in chromium and nickel but rich in iron. The matrix of the specimen was confirmed to be austenite and in the case of sample A with lattice parameter 3.47 Å (zone axis [011]), see Figure 3 b) position 3.
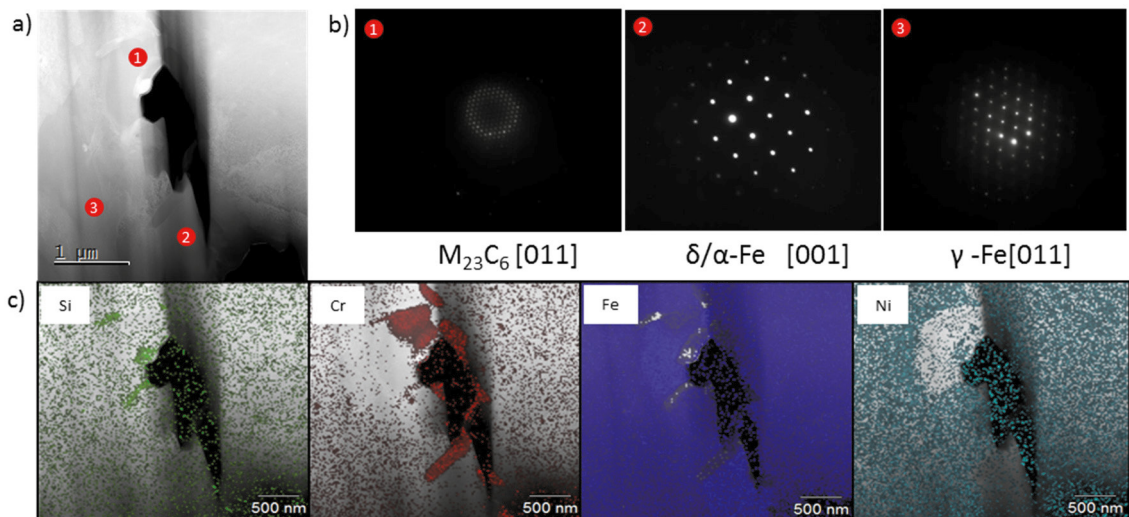

Fig. 3. a) Dark field TEM image containing a grain boundary across the image (specimen A). A cavity is shown in dark contrast b) diffraction pattern from selected areas c) EDS X-ray microanalyses of the same area.

Composition profiles were measured across the three secondary phase and the austenite boundaries. Only in the case of specimen A, the carbide-austenite boundary was enriched in phosphorus, Figure 4 a) (Martinez-Ubeda et al, 2016). The concentration in this particular interphase boundary is ~12wt% phosphorus. In the case of specimen B and C there was no evidence of such phosphorus segregation at any interphase, however, the Si-rich secondary phases showed P enrichment (Figure 4 b). Moreover, there was no enrichment at the austenite-austenite grain boundaries or the ferrite-austenite interphase boundaries in any specimen.

The prediction of secondary phases in equilibrium at 500°C were obtained using Thermo-Calc. Their mass fraction is included in table 3. The highest ferrite prediction is for sample A with a 0.51 mass fraction, followed by sample B and C. Similarly, for sigma prediction is slightly higher in sample A than B and C, only for 0.01 mass percent. The prediction of $M_{23}C_6$ is the same in the three samples with a 0.01 mass percent. Chi-phase was predicted to evolve only in sample A.
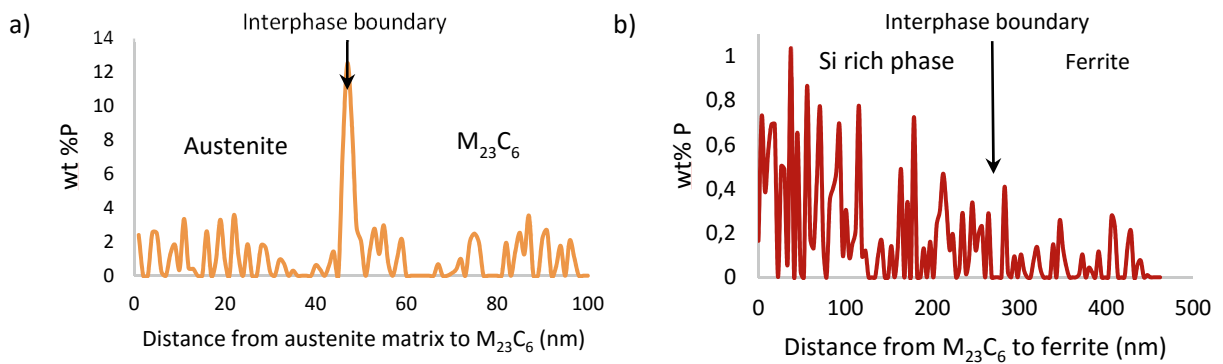

Fig. 4. Graph showing a) EDS profile from austenite matrix to $M_{23}C_6$ showing phosphorous segregation at the interphase boundary (specimen A) (Martinez-Ubeda, et al, 2016) and b) EDS profile from $M_{23}C_6$ to Si rich phase showing enrichment in phosphorous (specimen C).

Table 3. Mass fraction prediction (normalized to unit) from Thermo-Calc software using TCFE6 base data of secondary phases in equilibrium at 500°C.

	Mass fraction				
Sample	Austenite	Ferrite	$M_{23}C_6$	sigma	Chi
A	0.34	0.51	0.01	0.13	0.01
B	0.44	0.43	0.01	0.12	
C	0.45	0.41	0.01	0.12	

4. Discussion

After the statistical comparison, the three samples resulted significantly different in content of the main elements, with the biggest variation on Ni content in sample A. Accordingly, it can be stated that samples with same nominal composition of 316H may have statistically different elemental chemical composition. The implications of these differences in compositions may result in different precipitation kinetics or impurity segregation due to differences in the local composition.

Experimentally, the TEM analysis of specimen prepared in parent area, showed the same type of grain boundary precipitate in the three samples: ferrite, $M_{23}C_6$ and a Si rich phase (potentially G or R). δ-ferrite may be present from manufacturing but α-ferrite evolves during aging. The facts that ferrite was depleted in Cr and Ni but enriched in Fe, and, that the ferrite phases were in contact with $M_{23}C_6$, suggest that the ferrite was developed during service. It has

been proposed that the reduction of local activity of carbon would be the responsible for ferrite stabilization (Burnett et al, 2015).

The fraction area measured experimentally of ferrite and $M_{23}C_6$ are quite similar between samples, 0.3-0.4 % in case of ferrite and 0.2-0.3% for $M_{23}C_6$. However, Si rich precipitate was not quantified by EBSD because the size was under resolution limit. Sample A has less Si content than B and C, however it was the only one resulting in P segregation. Grain boundaries P segregation decreases the grain boundary cohesion producing embrittlement (Hong et al, 1986). If Si rich phase capture P, avoiding it grain boundary segregation, samples with higher Si content will easily tidy up all P and no further grain boundary segregation will occur. In this scenario sample A, with lower Si content, results grain boundary segregation.

The precipitation kinetic for 316H (Figure 1) above 600°C indicates that, $M_{23}C_6$ precipitate first, followed by the precipitation of the intermetallic phases (η, χ and σ). The precise sequence depends on the working temperature. Below 600°C only $M_{23}C_6$ is predicted in such diagram. However, ferrite has been seen experimentally to evolve during ageing in the analyzed samples, coincident with other workers (Burnet et al, 2015; White & Le May,1970; Park et al, 1968). This suggests that such evolution may happen after 10,000 h at 500°C, or that it is missed in the diagram. Si rich phases has been postulated to evolve from austenite and ferrite (Padilha & Rios, 2002; Shuro et al, 2012; Ecob et al, 1987). In the TEM results, the ferrite is adjacent to a $M_{23}C_6$ and the Si rich appears to nucleate in the ferrite corners. At 500°C, Figure 1 doesn't predict the evolution of intermetallic, matching with the experimental results.

At equilibrium all phases are stable and no further evolution occurs. Phase diagrams provide a useful guide to the phases present in stainless steel in equilibrium, however, they may not reflect the real state of the sample even after such a long periods of ageing as 150 kh. This situation is coincident with other workers work (Farneze et al, 2016), meaning the equilibrium has not been achieved yet for the samples studied. The diffusion at 500°C is so slow that only 0.3% of ferrite and $M_{23}C_6$ have evolved. Therfore, further evolution of precipitation is expected. Segregation is neither predicted by the equilibrium simulation.

The micro-hardness is a measure of the material resistance to localized plastic deformation where it has been observed empirically that hardness provides as an estimation of material's strength. The yield strength (in kgf/mm^2) is roughly a third of Vickers value. Yield stress can be used to provide macroscopic measurement of the internal creep resistance which depends on the movement of dislocation (Askeland, 1998). Dislocation mobility is controlled by solid solution and second phase precipitates (Park et al, 1968; Padilha & Rios, 2002). Both increase the critical resolved shear stress on the slip planes, increasing the material strength and therefore the macroscopic resistance to deformation. The lowest hardness value was found in parent of sample A, consistent with the hardness HAZ value, published elsewhere (Martinez-Ubeda et al, 2016). This difference with samples B and C may be based on the lower content of Ni (~2wt% lower than the other two samples) and therefore the lower strengthening by solid solution.

Evolution of secondary phases modifies creep deformation therefore it becomes important to understand the kinetic of the secondary evolution precipitation and the relationship of each phase promoting creep cavitation. The critical radius for cavity nucleation (equation 2) depends on the interfacial energy (γ'). P segregation decreases the interfacial energy and as a consequence promotes creep cavitation and modify creep failure. Components with such segregation may have reduced their creep life.

5. Conclusions

The main conclusions of this work are:

- Variation from cast to cast of AISI Type 316H lead to statistical different sample composition. Such differences in composition may have an effect on the evolution of secondary phases.
- Equilibrium simulation using Thermo-Calc do not coincide with the experimental results because at working temperature the samples have not reached the equilibrium.
- A difference in 2wt% in Ni shows a difference in the Yield Strength.
- Si may play an important role in P segregation and therefore in favoring creep cavity nucleation reducing creep life.

Acknowledgements

References

Askeland, D. R., Phulé, P. P., 1998. The Science and Engineering of Materials. ed. Stanley Thornes Ltd Publishers.

Burnett, T. L., Geurts, R., Jazaeri, H., Northover, S. M., McDonald, S. A, Haigh, S. J., Bouchard, P. J., Withers, P. J., 2015. Multiscale 3D Analysis of Creep Cavities in AISI Type 316 Stainless Steel. Materials Science and Technology 31(5), 522–534.

Challenger, K.D., Moteff, J., 1973. Quantitative Characterization of the Substructure of AISI 316 Stainless Steel Resulting from Creep. Metallurgical transactions 4(3), 749–55.

Chen, B., Hu, J. N., Flewitt, P. E. J., Smith, D. J., Cocks, A. C. F., Zhang, S. Y., 2014. Quantifying Internal Stress and Internal Resistance Associated with Thermal Ageing and Creep in a Polycrystalline Material. Acta Materialia 67, 207–219.

Chen, B., Spindler, M.W., Smith, D.J., Flewitt, P. E. J., 2010. A Review of the Effect of Thermo-Mechanical History on the Reheat Cracking in 316H Austenitic Stainless Steel Weldments. International journal of pressure vessels and pipings, 531–42.

Chen, B., 2011. Effects of Thermo Mechanical History on Creep Damage in 316H Austenitic Steel. PhD Thesis University of Bristol.

Dyson, B.F., 1983. Continuous Cavity Nucleation and Creep Fracture. Scripta Metallurgica 17(1), 31–37.

Ecob, R. C., Lobb, R. C., Kohler, V. L., 1987. The Formation of G-Phase in 20/25 Nb Stainless Steel AGR Fuel Cladding Alloy and its Effect on Creep Properties. Journal of Materials Science 22, 2867–2880.

Farneze, H. N., Tavares, S. S. M., Pardal, J. M., do Nascimento, R. F., de Abreu, H. F. G., 2016. Degradation of Mechanical and Corrosion Resistance Properties of AISI 317L Steel Exposed at 550ºC. Engineering Failure Analysis 61, 69–76.

Field, A. 2013. Discovering Statistics Using IBM SPSS Statistics. Third edition, Sage.

Giannuzzi, L. A., Stevie, F. A., 1999. A Review of Focused Ion Beam Milling Techniques for TEM Specimen Preparation. Micron 30, 197–204.

Hong, J. H., Nam, S. W., Choi, S.P., 1986. The Influences of Sulphur and Phosphorus Additions on the Creep Cavitation Characteristics in Type 304 Stainless Steels. Journal of Materials Science 21 (11), 3966–76.

Hsieh, C. C., Wu, W., 2012. Overview of Intermetallic Sigma σ Phase Precipitation in Stainless Steels. ISRN Metallurgy 2012(4), 1–16.

Intrater, J., Machlin, E. S., 1959. Grain Boundary Sliding and Intercrystalline Cracking. Acta Metallurgica 7(2), 140–143.

Lai, J.K.L., 1983. A Review of Precipitation Behaviour in AISI Type 316 Stainless Steel. Materials Science and Engineering 61, 101–9.

Lo, K.H., Shek, C.H., Lai, J.K.L., 2009. Recent Developments in Stainless Steels. Materials Science and Engineering R Reports 65(4-6), 39–104.

Martinez-Ubeda, A. I., Griffiths, I., Payton, O. D., Younes, C. M., Scott, T.B., Flewitt, P. E. J., 2016. Role of Long Term Ageing on the Creep Life of Type 316H Austenitic Stainless Steel Bifurcation Weldments. Pressure Vessels and Piping Division Conference.

Morris, D. G., Harries, D. R., 1978. Creep and Rupture in Type 316 Stainless Steel at Temperatures between 525 and 900°C Part I: Creep Rate. Metal Science 12(11), 525–31.

Padilha, A. F., Rios, P. R., 2002. Decomposition of Austenite in Austenitic Stainless Steels. ISIJ International 42(4), 325–327.

Park, S. H. C., Sato, Y. S., Kokawa, H., Okamoto, K., Hirano, S., and Inagaki, M., 1968. The Formatin of Ferrite and Sigma Phase in Some Austenitic Stainless Steel. Acta Metallurgica 16(12), 1441–1451.

Razali, N. M., Wah, Y. B., R., 2011. Power Comparisons of Shapiro-Wilk , Kolmogorov-Smirnov , Lilliefors and Anderson-Darling Tests. Journal of Statistical Modeling and Analytics 2(1), 21–33.

Seah, M. P., 1979. Surface Science in Metallurgy. Surface Science 80, 8–23.

Senior, B. A., 1990. Effect of Phase Transformations on the Creep Rupture Properties of two Type 316 Weld Metals. Journal of materials science 25, 45–53.

Shuro, I., Kuo, H. H., Sasaki, T., Hono, K., Todaka, Y., Umemoto, M., S., 2012. G-Phase Precipitation in Austenitic Stainless Steel Deformed by High Pressure Torsion. Materials Science and Engineering A 552, 194–198.

Warren, A.D., Griffiths, I.J., Harniman, R.L., Flewitt, P.E.J. and Scott, T.B., 2015. The Role of Ferrite in Type 316H Austenitic Stainless Steels on the Susceptibility to Creep Cavitation. Materials Science and Engineering A, 635.

Weiss, B.F., Strickler, R., 1972. Phase Instabilities during High Temperature Exposure of 316 Austenitic Stainless Steel. Metallurgical transactions 3(4), 851–66.

White W.E., Le May, I., 1970. Metallographic Observations on the Formation and Occurrence of Ferrite, Sigma Phase, and Carbides in Austenitic Stainless Steels Part II : Studies of AISI Type 316 Stainless Steel. Metallography 3, 51–60.